

Article

Investigation of Population Dynamics in 1.54- μm Telecom Transitions of Epitaxial $(\text{Er}_x\text{Sc}_{1-x})_2\text{O}_3$ Thin Layers for Coherent Population Manipulation: Weak Excitation Regime

Satoru Adachi ^{1,*} , Yoshihiro Kawakami ¹, Reina Kaji ¹, Takehiko Tawara ^{2,3} and Hiroo Omi ^{2,3}

¹ Division of Applied Physics, Graduate School of Engineering, Hokkaido University, Sapporo 060-8628, Japan; y_kawakami@eng.hokudai.ac.jp (Y.K.); r-kaji@eng.hokudai.ac.jp (R.K.)

² NTT Basic Research Laboratories, NTT Corporation, Atsugi, Kanagawa 243-0198, Japan; tawara.takehiko@lab.ntt.co.jp (T.T.); omi.hiroo@lab.ntt.co.jp (H.O.)

³ NTT Nanophotonics Center, NTT Corporation, Atsugi, Kanagawa 243-0198, Japan

* Correspondence: adachi-s@eng.hokudai.ac.jp; Tel.: +81-11-706-6709

Received: 13 April 2018; Accepted: 20 May 2018; Published: 25 May 2018

Abstract: We have investigated the energy transfers in the 1.54- μm region of $(\text{Er,Sc})_2\text{O}_3$ epitaxial thin films grown on Si(111). The interplay of the energy transfers between Er ions in the different and the same symmetry sites makes the dynamics complicated. To suppress the energy transfer upconversion, low power and resonant excitation of the third crystal-field level (${}^4I_{13/2} : Y'_3$) of the Er^{3+} site with C_{3i} symmetry was employed. The time-resolved photoluminescence measurements of the $Y'_1-Z'_1$ transition indicate the existence of two decay components having fast (10–100 μs) and slow (0.1–1 ms) relaxation times in the range of 4–60 K. The model calculation including the inter-site energy transfers, the temperature-sensitive and -insensitive non-radiative relaxations fits the experimental results well. Moreover, the long averaged inter- Er^{3+} distance obtained by decreasing Er concentration was found to reduce two kinds of non-radiative relaxation rates and the energy transfer rates between Er ions very effectively.

Keywords: erbium; epitaxial film; population dynamics

1. Introduction

Recently, there has been a great deal of interest in the subject of the population (and coherence) manipulation in quantum states, which provoked by the emergence of the quantum information paradigm [1,2]. The exciting researches are currently progressed in different solid-state systems such as semiconductor quantum dots [3–6] and nitrogen-vacancy centers in diamond [7,8] based on the interplay of the solid-state nature of the material engineering and the atom-like character of the sharp discrete energy levels. In those solid-state materials and structures, the techniques and concepts demonstrated previously in quantum optics of atoms and molecules [9–11] can be put to practical use.

Rare earth sesquioxides, R_2O_3 (R is rare earth), are alternative attractive candidates to exploit the coherent quantum phenomena because the intra- $4f$ transitions in rare-earth ions are weakly perturbed by the crystalline environments, and they exhibit a resonance with a very narrow inhomogeneous linewidth [12–15]. In the various R_2O_3 , we focus on the single crystalline $(\text{Er}_x\text{Sc}_{1-x})_2\text{O}_3$ including Er_2O_3 since the trivalent Er (Er^{3+}) can interact with a telecommunication-band photon ($\sim 1.5 \mu\text{m}$) and is a potential platform for the coherent population manipulation in the quantum information network using the well-developed infrastructure [15–20]. However, for this purpose, some obstacles have to be overcome: a relatively small oscillator strength of a single ion [21,22], a relatively large upconversion

(UC) rate [23–30], and a large concentration quenching [20,22]. These issues complicate the physics of the energy transfer (ET) in Er^{3+} -doped solids as well as in other R_2O_3 solids.

Figure 1 shows the various kinds of ET from one of the Stark levels in the ${}^4I_{13/2}$ manifold of Er^{3+} [30], which are observed in $(\text{Er}_x\text{Sc}_{1-x})_2\text{O}_3$ epitaxial thin films in this study. $(\text{Er}_x\text{Sc}_{1-x})_2\text{O}_3$ crystals have a cubic bixbyite structure (Figure 2a). A unit cell of the crystal contains 32 Er and/or Sc ions, 24 at sites with C_2 (non-inversion) symmetry and 8 at sites with C_{3i} (inversion) symmetry (denoted by C_2 and C_{3i} sites hereafter). In Er^{3+} in C_2 site, the (forced) electric-dipole transitions between the Stark levels are allowed. Since C_{3i} is a higher symmetry than C_2 , the electric-dipole transitions are forbidden strictly and only magnetic-dipole transitions between ${}^4I_{13/2} - {}^4I_{15/2}$ are allowed. Therefore, the UC occurs only in C_2 sites and gives rise to a severe population dissipation from a target state in the case of high power excitation [20]. Also, we observe mutual ET between Er^{3+} at C_2 and C_{3i} sites and the ET between Er^{3+} with the same site symmetry (C_2 or C_{3i}). In this work, we will refer to the former ET as the inter-site ET and the latter ET as the intra-site ET as shown in Figure 1. Moreover, the non-radiative relaxation occurs due to the crystal imperfection and multiple phonon emission. The intra-site ET induces the energy migration to open the channels to the quenching centers generated by the crystal defects and Er-ion clustering. By using the single crystalline $(\text{Er}_x\text{Sc}_{1-x})_2\text{O}_3$ with various Er concentrations, we can investigate how the inter-Er distance affects the energy flow in a system. Also, in order to investigate the energy flow in detail, the initial energy injection into well-resolved point such as one of the Stark levels in the multiplet is very important.

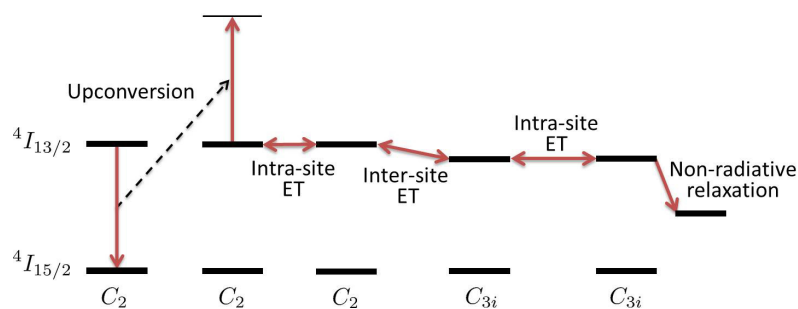


Figure 1. Various energy transfers that are observed in the transition between the Stark levels of ${}^4I_{15/2}$ and ${}^4I_{13/2}$ in the $(\text{Er}_x\text{Sc}_{1-x})_2\text{O}_3$ crystal. ET: energy transfer.

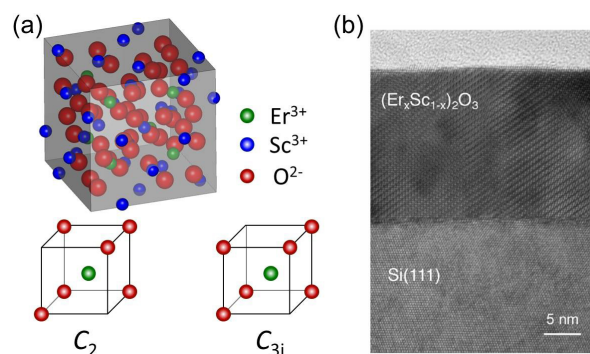


Figure 2. (a) Unit cell of bixbyite $(\text{Er}_x\text{Sc}_{1-x})_2\text{O}_3$ crystal. In this schematic, Er^{3+} at the C_2 site are replaced by Sc^{3+} . (lower panel) the configurations of C_2 and C_{3i} sites. (b) Cross-sectional transmission electron microscope (TEM) image of grown $(\text{Er}_x\text{Sc}_{1-x})_2\text{O}_3$.

In our previous study [17], we investigated the ETs in the Er_2O_3 single crystal under the resonant excitation of a Stark level (Y_2) in a C_2 site and estimated the large inter-site ET rate ($\sim 0.5 \mu\text{s}^{-1}$) and intra-site ET rate ($\sim 0.1 \mu\text{s}^{-1}$) via the excitation power dependence of the time-integrated photoluminescence (TI-PL) intensities, where the non-radiative relaxation and UC process were not explicitly taken into account. However, the energy dissipation via non-radiative relaxation and the UC process is supposed to affect the population dynamics greatly, and therefore, further detailed studies are necessary to reveal the population dynamics in a whole system.

In this study, we investigate the population dynamics in a whole system which consists of not only the inter- and intra-site ETs but the non-radiative relaxation in Er_2O_3 and $(\text{Er}, \text{Sc})_2\text{O}_3$ single crystals grown on Si(111). Since the UC process occurring in the C_2 site makes the population dynamics complicated, the low power resonant excitation of one of Stark levels (Y'_3) in the C_{3i} site is employed in order to minimize the effect of UC process. After deciding the proper experimental conditions, the time-resolved PL (TR-PL) measurements and their temperature dependence have directly revealed the ETs in the same site (C_{3i} , one of intra-site ET) and between the different sites ($C_{3i} \leftrightarrow C_2$, inter-site ET) by using three samples with different Er-concentrations. The simple model requires the temperature sensitive and insensitive non-radiative relaxations to reproduce the TR-PL signals and their temperature dependence well.

2. Samples and Experimental Setup

Er_2O_3 crystals have a lattice constant ($a = 10.54 \text{ \AA}$) which is almost twice one of Si(111) ($a = 5.43 \text{ \AA}$). Thus, the material is lattice-matched to Si(111) and can be epitaxially grown on Si with very low density of defects [31]. The averaged nearest neighbor distances of Er^{3+} between the C_2 - C_2 , C_2 - C_{3i} , and C_{3i} - C_{3i} sites are 1.945, 2.656, and 5.268 \AA , respectively. $(\text{Er}_x\text{Sc}_{1-x})_2\text{O}_3$ has similar properties and can also be epitaxially grown on a Si(111) substrate [18]. Sc_2O_3 is completely transparent for photons in the visible-to-telecom-band range [27]. Some of the Er^{3+} ions are replaced with Sc^{3+} ions to control the distance between the Er^{3+} ions as shown Figure 2a. $(\text{Er}_x\text{Sc}_{1-x})_2\text{O}_3$ crystals with $x = 0.012 - 1.000$ and the thickness of about 50 nm were grown on Si (111) surfaces with 7×7 reconstruction by molecular beam epitaxy at a growth temperature of 715 $^\circ\text{C}$, and were successfully to be single-crystalline [17,18], which was confirmed by the streak pattern of reflection high-energy electron diffraction. The cross-sectional image obtained with a transmission electron microscope (TEM) also indicated that the $(\text{Er},\text{Sc})_2\text{O}_3$ was epitaxially grown on the Si(111) surface in Figure 2b. The composition of the grown films was determined by Rutherford backscattering. An $\omega - 2\theta$ scan of the X-ray diffraction (XRD) measurements after growth (not shown here) also proved that single crystal $(\text{Er},\text{Sc})_2\text{O}_3$ layers were grown, and the crystal quality was approximately equivalent in all Er compositions [20]. Moreover, we found that the Er concentration-dependency of the lattice constant of $(\text{Er}_x\text{Sc}_{1-x})_2\text{O}_3$ satisfied Vegard's law. Thus, we can assume macroscopic uniformity of Er^{3+} distribution in the grown samples. The uniformity was supported also by the mapping of the PL spectra in the scanned area of $5 \times 5 \text{ mm}^2$ which indicated no change of the spectral properties (intensity, linewidth, and peak position) for all studied samples.

In this work, three $(\text{Er}_x\text{Sc}_{1-x})_2\text{O}_3$ samples with different Er-concentrations ($x = 1.000, 0.054,$ and 0.012) were studied. Please note that a large number of Er ions ($\sim 3 \times 10^{20} \text{ cm}^{-3}$) are still contained even in a sample $(\text{Er}_x\text{Sc}_{1-x})_2\text{O}_3$ with $x = 0.012$ (the lowest value in this work) compared to a commercial Er-doped fiber amplifier material (typically $< 10^{19} \text{ cm}^{-3}$). Hereafter, the samples with $x = 1.000, 0.054,$ and 0.012 are referred to as Sample A, B, and C, respectively. The Er^{3+} density, number of Er^{3+} in unit cell, averaged inter- Er^{3+} , and intra (inter) site distance of the studied $(\text{Er}_x\text{Sc}_{1-x})_2\text{O}_3$ samples are summarized in Table 1.

As shown in Figure 3a, Er^{3+} has the optical transition between the first excited state ($^4I_{13/2}$ manifold with Stark levels $Y_i^{(l)}, i = 1 - 7$, labeled from lower to higher energy level) and the ground state ($^4I_{15/2}$ manifold with Stark levels $Z_j^{(l)}, j = 1 - 8$), which exhibits the photon emission and absorption at around 1.5 μm -region. The (forced) electric-dipole transitions between the Stark levels

are allowed for Er^{3+} in C_2 sites ($Y_i - Z_j$), while only magnetic-dipole transitions are possible for Er^{3+} in C_{3i} sites ($Y'_i - Z'_j$). Since Sc_2O_3 is transparent in the visible to telecommunication-band region, the emission and absorption at around $1.5 \mu\text{m}$ in $(\text{Er}_x\text{Sc}_{1-x})_2\text{O}_3$ originate from Er ions.

The as-grown samples were mounted in a continuous He-flow cryostat, and the temperature was controlled. A continuous-wave tunable laser (1470–1560 nm, spectral width of 400 kHz) with an erbium-doped fiber amplifier was used to excite the $^4I_{13/2}$ manifold. Since the bandwidth of the excitation laser was much narrower than the energy intervals in the $^4I_{13/2}$ manifold, the resonant excitation of one Stark level was possible.

In the TI-PL measurements, the PL peaks in the $1.54\text{-}\mu\text{m}$ (visible) wavelength regions were detected by InGaAs-photodiode array (Si-CCD) through the monochromator under the $^4I_{13/2}$ manifold excitation by varying the sample temperature 4–150 K. The excitation laser was focused on a sample surface with the diameter of $\sim 15 \mu\text{m}$ by an objective lens, and the incident angle was set to be 45° from the sample growth axis. Avoiding a strong stray light, the PL signal was collected perpendicularly by an another objective lens with a numerical aperture of 0.4. The total spectral resolution was about $60 \mu\text{eV}$ for the TI-PL measurements.

For the TR-PL measurements, a pulsed excitation formed from the continuous-wave laser light by an acousto-optic modulator and a streak camera (model C11293S, Hamamatsu Photonics, Hamamatsu, Japan) were used to observe the temporal evolution of PL signals from $^4I_{13/2}$ manifold, and the sample temperature was changed around 4–60 K. The spectral and temporal resolutions of the TR-PL measurement system were $500 \mu\text{eV}$ and 20 ps (for a 1 ns time range), respectively.

Table 1. Summary of the studied $(\text{Er}_x\text{Sc}_{1-x})_2\text{O}_3$ samples. The averaged distances are evaluated from the lattice constant and Er concentration.

Sample	x	Er^{3+} Density (cm^{-3})	Er^{3+} in Unit Cell	Averaged Inter- Er^{3+} Distance (\AA)	Averaged Intra(inter)-Site Distance		
					C_2 - C_2 (\AA)	C_{3i} - C_{3i} (\AA)	C_2 - C_{3i} (\AA)
A	1.000	2.7×10^{22}	32	3.3	1.95	5.27	2.66
B	0.054	1.4×10^{21}	1.6	8.8	5.15	13.94	7.03
C	0.012	3.4×10^{20}	0.4	14.5	8.50	23.01	11.60

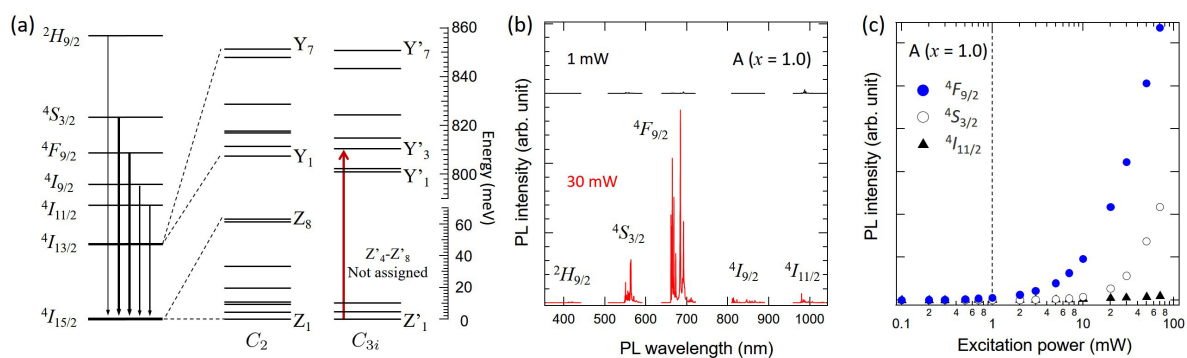


Figure 3. (a) Schematic of the energy levels of Er^{3+} and the closeup views of $^4I_{13/2}$ and $^4I_{15/2}$ manifolds (after reference [21]). (b) The upconversion photoluminescences (UC-PLs) from various manifolds in Sample A with $P_{\text{exc}} = 30 \text{ mW}$ (lower panel, red) and $P_{\text{exc}} = 1 \text{ mW}$ (upper panel, black) under Y'_3 resonant excitation ($\lambda_{\text{exc}} = 1530.5 \text{ nm}$) at 4 K. The PL intensities are scaled relatively between both P_{exc} . (c) Excitation power dependences of the UC-PL intensities corresponding to the three manifolds, $^4F_{9/2}$ (solid circles), $^4S_{3/2}$ (open circles), and $^4I_{11/2}$ (triangles) in Sample A.

3. Results and Discussions

One of the important ET processes for fundamental and application aspects is known as UC process in the Er-doped materials [30]. The UC process brings a severe reduction in the population of the target energy level, and it also makes the population dynamics in the considered system complicated. We seek the proper condition to avoid the UC process effectively from the excitation power dependence of TI-PL signals before studying the population dynamics in detail.

3.1. Time-Integrated Photoluminescence Measurements

The UC-PL means the photon emission with shorter wavelength than that of the excitation laser, and it comes from the excited-state absorption and/or the cooperative UC (Auger UC) in which the excitation into a higher lying state and de-excitation to a lower lying state occur simultaneously as shown in Figure 1. The UC levels of Er^{3+} in C_2 sites were summarized in Figure 3a, and Figure 3b shows examples of the UC-PL spectra observed in Sample A: 4 K under Y'_3 resonant excitation, the excitation powers (P_{exc}) of 1 mW (upper panel) and 30 mW (lower panel). While the observed UC-PLs were negligible at $P_{\text{exc}} = 1$ mW, the UC-PLs from various manifolds such as $^4S_{3/2}$ (~ 550 nm), $^4F_{9/2}$ (~ 680 nm), $^4I_{9/2}$ (~ 850 nm), and $^4I_{11/2}$ (~ 1000 nm) were observed clearly at $P_{\text{exc}} = 30$ mW. Especially, the UC-PLs from $^4F_{9/2}$ and $^4S_{3/2}$ manifolds were much stronger than other UC-PLs.

Figure 3c shows the excitation power dependences of the integrated UC-PL intensities from $^4F_{9/2}$, $^4S_{3/2}$, and $^4I_{11/2}$ to $^4I_{15/2}$ manifolds. It clearly indicates that the appearance of the UC-PLs requires more than a critical excitation power, and the UC-PLs become remarkable in the high power excitation region. Additionally, we found a similar power dependence of the UC-PLs in Samples B and C, and the clear but weaker UC-PLs were observed at more than the similar critical excitation power with that in Sample A (not shown here). Therefore, the influence of the UC process is considered to be negligible in the low power excitation region of 0.1–a few mW. All the measurements in the following experiments were carried out under the low power excitation condition ($P_{\text{exc}} = 1$ mW). Please note that the observed UC-PLs can be addressed to the transitions from the higher-lying manifolds in C_2 sites although the excitation laser was tuned to the Y'_3 resonance in C_{3i} sites. The assignment of UC-PLs is also supported by the fact that the optical transitions between the higher-lying states and the ground states in C_{3i} sites are forbidden [21]. Thus, the appearance of UC-PLs indicates the presence of the inter-site ET process ($C_{3i} \rightarrow C_2$) in the $^4I_{13/2}$ manifold.

Under the low power excitation condition ($P_{\text{exc}} = 1$ mW), we study the inter-site ET process and the thermal quenching of PL spectra. Figures 4a–c show the TI-PL spectra at some different temperatures under the resonant excitation of the Y'_3 level for Samples A, B, and C, respectively. The strongest PL spectra at 1548 nm in Sample A corresponds to the transition between $Y'_1 - Z'_1$ (C_{3i} site). The transition energy of the peak shifts to ~ 1551 nm in Samples B and C because the crystal field surrounding Er^{3+} is changed by decreasing the Er concentration. Despite the resonant excitation to the $Y'_3 - Z'_1$ transition in C_{3i} , the PL peaks that were assigned to be the transitions $Y_1 - Z_1$ and $Y_1 - Z_2$ in C_2 sites appeared along with $Y'_1 - Z'_1$ transition in C_{3i} sites. The observation evidently indicates that the energy transfer from C_{3i} to C_2 occurs. Please note that the PL intensities from C_2 sites in the low Er-concentration samples B and C become weaker than those in Sample A. These results show that the interaction between Er ions and the resultant inter-site ET process can be reduced by the extension of the averaged inter-ionic distance through decreasing the Er-concentration. Actually, the averaged value of the inter-site distance of Er^{3+} , $R_{C_2-C_{3i}}$ extends from 2.66 Å to 7.03 (11.6) Å as the Er-concentration is reduced from $x = 1.000$ to 0.054 (0.012) in Sample A to B (C) as shown in Table 1.

Other important information about the inter-site ET process is found from the photoluminescence excitation (PLE) measurement as shown in Figure 4d where the excitation wavelength was swept around $^4I_{13/2}$ manifold (1520–1555 nm). At the Y'_1 resonant excitation ($\lambda_{\text{exc}} = 1548$ nm), the PL signal of $Y_1 - Z_1$ transition (1535 nm) was observed. Accordingly, the $Y'_1 \rightarrow Y_1$ transition seems to be a dominant process relevant to the $C_{3i} \rightarrow C_2$ ET rather than the $Y'_3 \rightarrow Y_1$ transition, and the inter-site ET occurs after the rapid internal energy relaxation in C_{3i} sites (i.e., $Y'_3 \rightarrow Y'_1 \rightarrow Y_1$). Further, it should be noted

that the strong PL of the $Y'_1-Z'_1$ transition (1548 nm) appeared at the Y_1 and Y_2 resonant excitation; it denotes the presence of the inter-site ET in the reverse direction ($C_2 \rightarrow C_{3i}$).

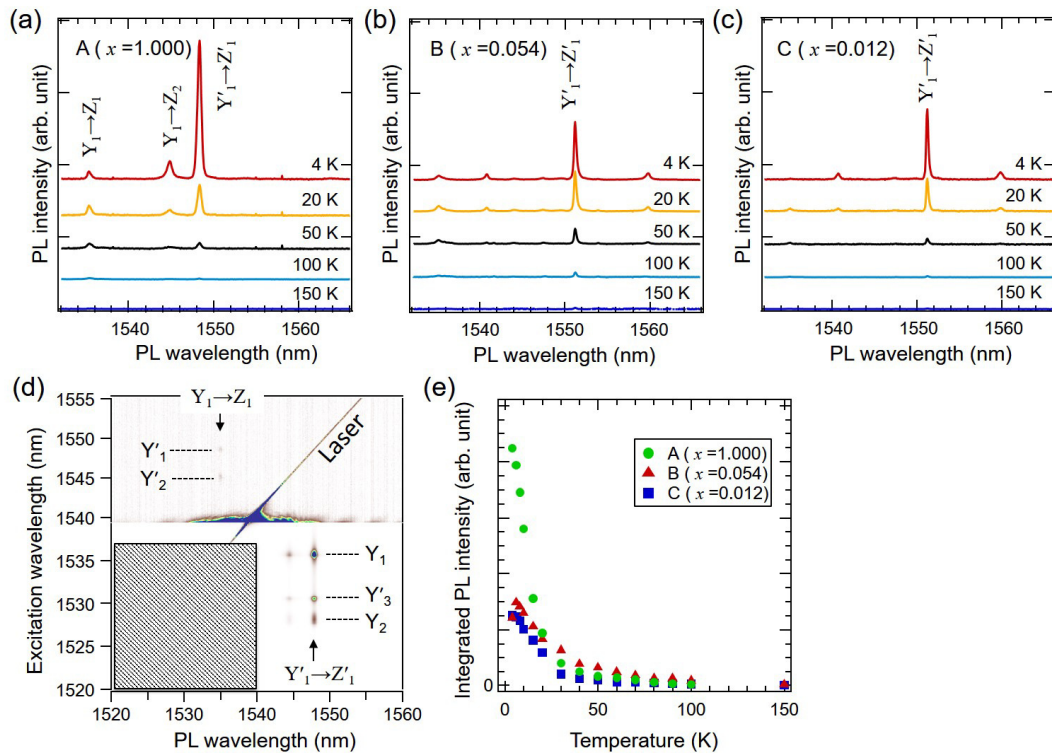


Figure 4. Time-integrated photoluminescence (TI-PL) spectra at different temperatures for the $(Er_xSc_{1-x})_2O_3$ crystals (a) Sample A ($x = 1.000$), (b) Sample B ($x = 0.054$), and (c) Sample C ($x = 0.012$) under the $Y'_3-Z'_1$ resonant excitation with $P_{exc} = 1$ mW. (d) The 2D plot of PLE spectra where the excitation laser was swept around the ${}^4I_{13/2}$ manifold in Sample A at 4 K. In the excitation region of 1520–1540 nm, the PLs below 1540 nm as depicted by a gray square are blocked by a low-pass filter. (e) The temperature dependence of the TI-PL intensities of the $Y'_1-Z'_1$ transitions shown in (a–c) is plotted: Samples A (circles), B (triangles), and C (squares).

For the energy transfer mechanisms between Er ions, the Förster type (dipole-dipole interaction) and Dexter type (wave-function overlapping) are well known from the previous studies [32,33], and the former and the latter are proportional to R^{-6} and $\exp(-2R/L)$, respectively (R : the inter-ionic distance, L : the van der Waals radius). In our case, the remarkable suppression by extending $R_{C_2-C_{3i}}$ and the energy mismatch between Y'_1 and Y_1 levels of ~ 7 meV suggest that the Dexter-type mechanism, which is more sensitive to the change in R than the Förster-type mechanism, seems to be dominant in the inter-site ET process.

Figure 4e shows the temperature dependence of the TI-PL intensities of the $Y'_1-Z'_1$ transition in Figure 4a–c for the three samples. In Sample A, a significant thermal quenching of the PL intensity (I_{PL}) occurs till around 20 K, and the I_{PL} at 20 K is reduced approximately to the one-quarter of I_{PL} at 4 K. In contrast, the decrease in PL intensities in Samples B and C are more moderate; the I_{PL} at ~ 20 K is about a half of I_{PL} at 4 K. These behaviors appear clearly in the values of non-radiative recombination rate W_{nr}^0 (or time τ_{nr}^0) in Table 2, which is deduced from the time-resolved PL measurements in the next subsection. The data suggests that the extension of the inter-ionic distance serves as a suppression of the thermal quenching as well as the reduction in the inter-site ET. The suppression of the thermal quenching in Samples B and C may come from the reduction of the possibility to reach non-radiative centers due to the reduction in the inter-site ET. The dilution of Er ions replacing by Sc ions induces

the increase of the lattice mismatch since the lattice constant of Sc_2O_3 is 9.85 \AA , and thus the increase of the defect density may be expected. However, the PL intensity in Sample C does not change and is even stronger than that in Sample B as shown in Figure 4b,c. This observation leads to the conclusion that the change of the defect density via the lattice mismatch due to the change of x does not have a significant effect. We consider that the extension of the inter-Er distance by replacing Er with Sc is more effective to suppression of the non-radiative recombination rather than the increase of non-radiative centers via the induced lattice mismatching.

In this section, we obtained the following findings about the energy transfers in $(\text{Er}_x\text{Sc}_{1-x})_2\text{O}_3$ crystals under the resonant excitation of the Y'_3 level:

1. The UC process occurring in C_2 sites is negligible under a low power excitation condition of $P_{\text{exc}} < \text{a few mW}$.
2. The inter-site ET occurs mutually between the lowest states of Y'_1 and Y_1 , and it follows the internal energy relaxation in C_{3i} sites ($Y'_3 \rightarrow Y'_1$).
3. The extension of the inter- Er^{3+} distance is very effective in suppressing the inter-site ET and thermal quenching.

These findings will help to construct the model of population dynamics in the target energy levels of Er-ions.

Table 2. Summary of the fitting parameters to reproduce the temperature dependence of τ_{slow} depicted in Figure 6d.

Sample	Er^{3+} x	E_A (meV)	A_r (ms^{-1})	τ_r (ms)	W_{nr}^0 (ms^{-1})	τ_{nr}^0 (ms)
A	1.000	1.02	3.92	0.255	122	0.008
B	0.054	9.01	0.88	1.14	8.08	0.124
C	0.012	2.89	0.56	1.78	2.70	0.370

3.2. Time-Resolved Photoluminescence Measurements

The population dynamics can be reflected more directly in TR-PL signals. In this section, we investigate the decay dynamics of the PL signal corresponding to the Y'_1 - Z'_1 transition and its temperature dependence ($T = 4\text{--}60 \text{ K}$) under the Y'_3 resonant excitation at $P_{\text{exc}} = 1 \text{ mW}$.

Figure 5 shows the TR-PL signals of the Y'_1 - Z'_1 transition in the three samples at (a) 6 K and (b) 20 K in one instance. Though the signal in Sample A decays in one order faster than those in Samples B and C, all the TR-PL signals for each Er-concentration and each temperature could be decomposed into two components by the double exponential fitting: fast decay and slow decay components with characteristic times τ_{fast} and τ_{slow} . Please note that the solid curves in the figures represent the calculated results based on the population dynamics model discussed in the next section.

The relaxation times τ_{fast} and τ_{slow} deduced from the double exponential fitting are plotted as a function of the temperature for Samples A, B, and C in Figure 6a–c, respectively. As a whole, we note that both τ_{fast} and τ_{slow} get shorter with increasing Er-concentration. As clearly shown in the figures, while the τ_{fast} is insensitive to the change in temperature and is almost constant in the temperature range 4–60 K, the τ_{slow} shows a rapid reduction with increasing temperature; These behaviors are similarly observed in all three samples.

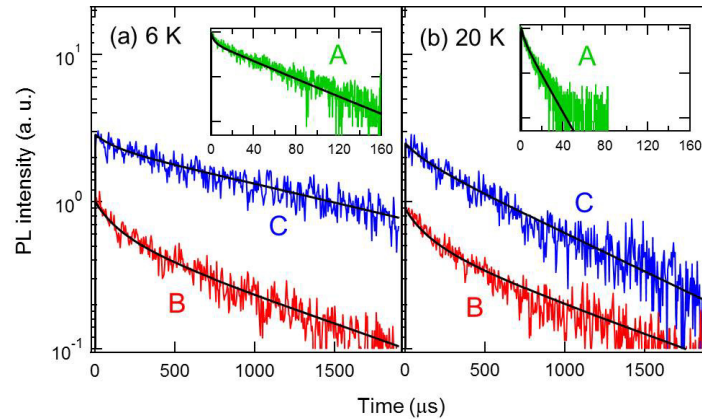


Figure 5. Time-resolved-PL signals of the $Y_1' - Z_1'$ transition at (a) 6 K and (b) 20 K. Insets are the logarithmic plots of PL intensities in Sample A. The signals of Sample B are shifted down for eye-friendly plots. The double exponential decays with characteristic relaxation times, τ_{fast} and τ_{slow} , are clearly observed for all the samples and temperatures. The solid curves are the calculations based on the population dynamics model in Section 3.3.

First, we focus on the τ_{slow} , which is assumed to include the two different decay components, the radiative and the non-radiative relaxations. Since the radiative relaxation rate is determined quantum-mechanically and is independent of temperature in principle, we consider that the temperature-sensitive property of τ_{slow} component is caused by the thermally-activation type non-radiative relaxation process. The τ_{slow} can be expressed as a sum of the rates of radiative and thermally-activation type non-radiative relaxations:

$$\frac{1}{\tau_{slow}} = A_r + W_{nr}^0 \exp\left(-\frac{E_A}{k_B T}\right), \quad (1)$$

where A_r is the radiative relaxation rate, W_{nr}^0 is the non-radiative relaxation rate at 0 K, k_B is the Boltzmann constant, and E_A is the activation energy of the non-radiative center. Figure 6d shows the observed τ_{slow} and the fitting curves as a function of the inverse temperature, and the fitting parameters are summarized in Table 2, where the radiative and non-radiative relaxation times, $\tau_r = 1/A_r$ and $\tau_{nr}^0 = 1/W_{nr}^0$, are also listed. Remarkably, the characteristic parameter for the thermally-activation type non-radiative relaxation process, W_{nr}^0 is strongly reduced to $\sim 1/30$ by decreasing the Er-concentration from $x = 1.000$ to $x = 0.012$. This is because the longer inter- Er^{3+} distance suppresses the inter-site and/or the intra-site ET process and prevents the photo-excited electrons from being captured in the quenching centers consequently.

In Table 2, there is also a difference in the radiative rate A_r between the low and high Er-concentration samples. In Samples B and C, the experimentally deduced A_r almost agrees with the theoretically estimated values [34,35] which was obtained by using the Judd-Ofelt parameters Ω_t ($t = 2, 4, 6$) in $(Er_x, Sc_{1-x})_2O_3$ transparent ceramics with $x = 0.003$ [36]. On the other hand, a larger A_r was observed in Sample A, and it suggests the increase in the *effective* transition dipole moment. The smaller inter- Er^{3+} distance achieved in high Er-concentration crystals enhances the Er-Er interaction and may induce a larger coherence volume [37] as one plausible candidate. It can lead to a larger effective dipole moment, and thus, to a larger radiative relaxation rate compared with those in low Er-concentration systems.

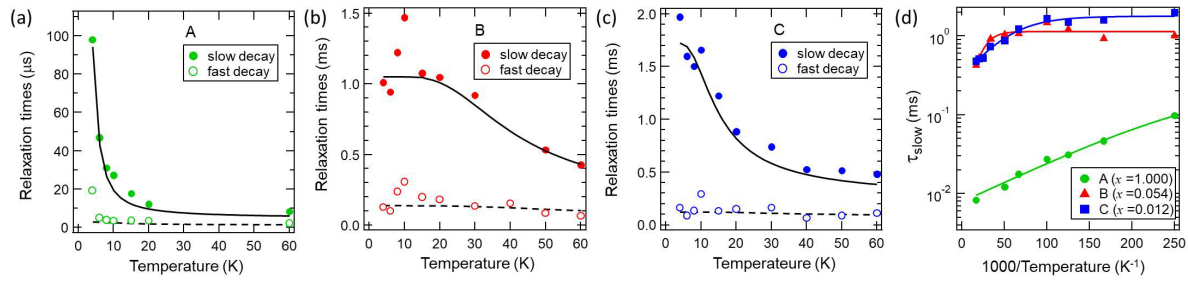


Figure 6. Temperature dependences of the relaxation times, τ_{fast} (open circles) and τ_{slow} (solid circles), for the three samples; (a) A: $x = 1.000$, (b) B: $x = 0.054$, and (c) C: $x = 0.012$. The solid and dashed lines are results of model calculation. (d) Arrhenius plot of τ_{slow} in Sample A (circles), B (triangles), and C (squares). The solid lines are the fittings by using Equation (1).

Next, we mention the origin of the fast, temperature-insensitive decay. Since the radiative relaxation process is included in the τ_{slow} , the τ_{fast} is determined only by the non-radiative relaxation process. At this stage, we suppose that the non-radiative energy dissipation from the Y'_1 level due to the multi-phonon (MP) emission process to the quenching centers is one candidate for the τ_{fast} component. The MP relaxation time τ_{MP} ordinarily depends on the sample temperature, and it is proportional to the following factor, $[1 - \exp(-E_p/k_B T)]^{-m}$ in the single frequency model, where E_p is the phonon energy and m is the number of phonons, respectively [38]. Since the E_p in Sc_2O_3 is about 74 meV [18] and the corresponding one in $(\text{Er}, \text{Sc})_2\text{O}_3$ crystal seems to be close with that, the MP relaxation rate for $m = 1-15$ is insensitive to the change in temperature below 100 K, and it agrees qualitatively with the behavior of the experimentally obtained τ_{fast} .

3.3. Model Calculations

To reproduce the TR-PL signals and their temperature dependences observed in Section 3.2, we consider the energy transfer model shown in Figure 7 and solve the following rate equations:

$$\frac{dn_0}{dt} = -\Gamma n_0 + A_r n_1 - C_{41} n_4 n_0 + C_{14} n_3 n_1, \quad (2)$$

$$\frac{dn_1}{dt} = W_{21} n_2 - (A_r + W_{\text{nr}}) n_1 - \left(1 - \frac{n_d}{N_d}\right) W_d n_1 + C_{41} n_4 n_0 - C_{14} n_3 n_1, \quad (3)$$

$$\frac{dn_2}{dt} = \Gamma n_0 - W_{21} n_2, \quad (4)$$

$$\frac{dn_d}{dt} = \left(1 - \frac{n_d}{N_d}\right) W_d n_1, \quad (5)$$

$$\frac{dn_3}{dt} = \frac{n_4}{\tau_{43}} + \frac{n_5}{\tau_{53}} + C_{41} n_4 n_0 - C_{14} n_3 n_1 + C_{45} n_4^2, \quad (6)$$

$$\frac{dn_4}{dt} = -2C_{45} n_4^2 - \frac{n_4}{\tau_{43}} + \frac{n_5}{\tau_{54}} - C_{41} n_4 n_0 + C_{14} n_3 n_1, \quad (7)$$

$$\frac{dn_5}{dt} = C_{45} n_4^2 - \frac{n_5}{\tau_{53}} - \frac{n_5}{\tau_{54}}, \quad (8)$$

where n_i is the population probability of the level labeled i ($i = 0-5, d$), Γ is the pumping rate, C_{14} and C_{41} are the inter-site ET rate between the states 1 (Y'_1) and 4 (Y_1), and C_{45} is the upconversion rate in C_2 sites from 4 to 5 (UC levels) states. In this model, the cross-relaxation and Auger process are assumed for inter-site ET and UC, respectively. For state 1, the radiative relaxation rate A_r is explicitly introduced and the radiative and non-radiative relaxation processes are definitely distinguished; by contrast, the lifetimes of states 4 and 5, τ_{43} , τ_{54} , and τ_{53} are determined by both the radiative and

non-radiative relaxation processes (i.e., level lifetimes). The rapid internal relaxation from states 2 to 1 ($Y'_3 \rightarrow Y'_1$) with a rate W_{21} follows the optical pumping to state 2 with a rate Γ .

In our model, two kinds of non-radiative relaxation processes, the temperature-sensitive relaxation with a rate W_{nr} and the temperature-insensitive relaxation with a rate W_d are considered for state 1. Here, the rate W_{nr} has the thermally-activation type as similar to the τ_{slow} process in Section 3.2, and it can be written as $W_{nr} = W_{nr}^0 \exp(-E_A/k_B T)$. Further, the temperature-insensitive non-radiation relaxation process with W_d needs to have the density-of-state limitation property as shown in Equation (5) in order to reproduce the double exponential decay curve. Although the UC process is one of the candidates to induce the double exponential decay, it can be negligible in our experimental condition with a low excitation power, especially for the low Er-concentration Samples B and C. The energies via these non-radiative relaxations are dissipated from the considered system. Additionally, the UC rate C_{45} is set to zero because the TR-PL measurements were carried out under the low power excitation condition and the effect of the UC process was negligible.

The calculated results deduced from the temporal profile of n_1 were depicted as solid curves in Figure 5. The parameters about W_{nr} and A_r were estimated from the corresponding ones listed in Table 2, and the set of parameters used in the rate equation analysis was summarized in Table 3. As clearly shown, the calculations can reproduce the experimental results for all the samples, and their temperature dependences are described well in the framework of our model, that is, the assumed W_{nr} works adequately to describe the thermal quenching of the Y'_1 - Z'_1 emissions. In addition, we extracted two relaxation times corresponding to the fast and slow decay components from the calculated curves of n_1 , and we plotted them in Figure 6a–c as solid and dashed lines. The extracted relaxation times show the similar temperature dependences with the experimentally obtained ones. The agreements between the experimental and calculated results support the validities of our model and assumptions, and the model calculations successfully explain the energy transfers and its temperature dependence especially of the target energy level Y'_1 .

Further, the other non-radiative relaxation rate, W_d can also estimated as listed in Table 3, and the W_d in Sample C is reduced to 1/70 of W_d in Sample A. It is found that the reduction of Er-concentration is effective to suppress the temperature-insensitive non-radiative rate as well as the temperature sensitive non-radiative rate.

Although the excellent agreement between the observations and model calculations by a simple model in Figure 7 was obtained, some assumptions and the parameters that have not been obtained experimentally were used. Therefore, further detail experimental investigation to specify the physical origins of those non-radiative relaxations and the analysis by the microscopic theory such as Inokuti-Hirayama model [39,40] are required.

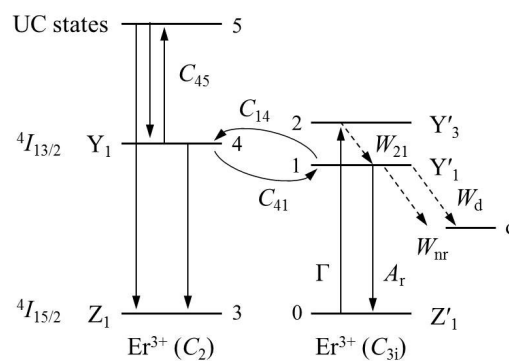


Figure 7. Energy diagram for the rate equation analysis compose of the ground (Z_1, Z'_1), the first excited (Y_1, Y'_1, Y'_3), and the UC states.

Table 3. The set of parameters used in the rate equation analysis.

Er ³⁺ <i>x</i>	$Y_1 \rightarrow Z_1$	$Y'_1 \rightarrow Z'_1$	$Y'_1 \rightarrow Y_1$	$Y_1 \rightarrow Y'_1$	Non-Radiative Decays from Y'_1		
	τ_{43} (ms)	τ_r (ms)	$1/C_{14}$ (ms)	$1/C_{41}$ (ms)	τ_{nr}^0 (ms)	W_d (s ⁻¹)	N_d
1.000	0.10	0.26	1.00	0.008	0.006	1.0×10^5	0.4
0.054	1.59	1.18	500	30.3	0.160	3.3×10^3	0.4
0.012	1.30	1.75	2×10^3	167	0.300	1.4×10^3	0.4

4. Summary

In summary, we have investigated the temperature dependence of the PL intensity and lifetime in (Er_{*x*}Sc_{1-*x*})₂O₃ (*x* = 1.0, 0.054, 0.012) epitaxial thin films grown on Si(111) under the excitation conditions that the energy transfer upconversion process from C₂ site is minimized; resonant excitation of the third Stark level (⁴I_{13/2}: Y₃) with a low power was employed. The extension of the averaged inter-Er distance by replacing Er with Sc is more effective to suppression of the non-radiative recombination rather than the increase of non-radiative centers via the induced lattice mismatching. In addition, thermal quenching could be greatly suppressed. These observations lead to the conclusion that the extension of inter-Er distance suppresses the energy transfers in inter and intra Er sites and reduces the captured possibility by the quenching centers. The simple model calculation introducing the inter-site ET, the temperature-sensitive and -insensitive non-radiative relaxations explains well the temperature dependence of the relaxation times as well as the time-resolved PL signals. The obtained results contribute to the coherent population manipulation and development of highly efficient optical devices on Er-related materials on Si substrates.

Author Contributions: Y.K., T.T., and S.A. conceived and designed the experiments; Y.K. and T.T. performed the experiments; Y.K., R.K. and S.A. analyzed the data; H.O. supplied the high quality samples; S.A. wrote the paper.

Acknowledgments: The authors would like to acknowledge H. Gotoh, A. Najar, and M. Ijspeert (NTT Basic Research Laboratories) for fruitful discussions and careful reading. This work was supported in part by JSPS KAKENHI (Grants No. JP25247047 and JP16H03821).

Conflicts of Interest: The authors declare no conflict of interest. The funding sponsors had no role in the design of the study; in the collection, analyses, or interpretation of data; in the writing of the manuscript, and in the decision to publish the results.

References

1. Awschalom, D.D.; Samarth, N.; Loss, D. (Eds.) *Semiconductor Spintronics and Quantum Computation*; Springer: Berlin, Germany, 2002; ISBN 978-3-642-07577-3.
2. Slavcheva, G.; Roussignol, P. (Eds.) *Optical Generation and Control of Quantum Coherence in Semiconductor Nanostructures*; Springer Series in NanoScience and Technology; Springer: Berlin, Germany, 2010; ISBN 978-3-642-12490-7.
3. Bonadeo, N.H.; Erland, J.; Gammon, D.; Park, D.; Katzer, D.S.; Steel, D.G. Coherent optical control of the quantum state of a single quantum dot. *Science* **1998**, *282*, 1473–1476. [[CrossRef](#)] [[PubMed](#)]
4. Press, D.; Ladd, T.D.; Zhang, B.; Yamamoto, Y. Complete quantum control of a single quantum dot spin using ultrafast optical pulses. *Nature* **2008**, *456*, 218–221. [[CrossRef](#)] [[PubMed](#)]
5. De Greve, K.; McMahon, P.L.; Press, D.; Ladd, T.D.; Bisping, D.; Schneider, C.; Kamp, M.; Worschech, L.; Hofling, S.; Forchel, A.; et al. Ultrafast coherent control and suppressed nuclear feedback of a single quantum dot hole qubit. *Nat. Phys.* **2011**, *7*, 872–878. [[CrossRef](#)]
6. Greilich, A.; Carter, S.G.; Kim, D.; Bracker, A.S.; Gammon, D. Optical control of one and two hole spins in interacting quantum dots. *Nat. Photonics* **2011**, *5*, 702–708. [[CrossRef](#)]
7. Dutt, M.V.G.; Childress, L.; Jiang, L.; Togan, E.; Maze, J.; Jelezko, F.; Zibrov, A.S.; Hemmer, P.R.; Lukin, M.D. Quantum register based on individual electronic and nuclear spin qubits in diamond. *Science* **2007**, *316*, 1312–1316. [[CrossRef](#)] [[PubMed](#)]
8. Fuchs, G.D.; Burkard, G.; Klimov, P.V.; Awschalom, D.D. A quantum memory intrinsic to single nitrogen-vacancy centres in diamond. *Nat. Phys.* **2011**, *7*, 789–793. [[CrossRef](#)]

9. Boozer, A.D.; Boca, A.; Miller, R.; Northup, T.E.; Kimble, H.J. Reversible state transfer between light and a single trapped atom. *Phys. Rev. Lett.* **2007**, *98*. [[CrossRef](#)] [[PubMed](#)]
10. Ritter, S.; Nölleke, C.; Hahn, C.; Reiserer, A.; Neuzner, A.; Uphoff, M.; Mücke, M.; Figueroa, S.; Bochmann, J.; Rempke, G. An elementary quantum network of single atoms in optical cavities. *Nature* **2012**, *484*, 195–200. [[CrossRef](#)] [[PubMed](#)]
11. Stute, A.; Casabone, B.; Brandstätter, B.; Friebe, K.; Northup, T.E.; Blatt, R. Quantum-state transfer from an ion to a photon. *Nat. Photonics* **2013**, *7*, 219–222. [[CrossRef](#)] [[PubMed](#)]
12. Böttger, T.; Thiel, C.W.; Cone, R.L.; Sun, Y. Effects of magnetic field orientation on optical decoherence in $\text{Er}^{3+}:\text{Y}_2\text{SiO}_5$. *Phys. Rev. B* **2009**, *79*. [[CrossRef](#)]
13. Thiel, C.W.; Böttger, T.; Cone, R.L. Rare-earth-doped materials for applications in quantum information storage and signal processing. *J. Lumin.* **2011**, *131*, 353–361. [[CrossRef](#)]
14. Ter-Gabrielyan, N.; Fromzel, V.; Dubinskii, M. Performance analysis of the ultra-low quantum defect $\text{Er}^{3+}:\text{Sc}_2\text{O}_3$ laser. *Opt. Mater. Express* **2011**, *1*, 503–513. [[CrossRef](#)]
15. Tawara, T.; Mariani, G.; Shimizu, K.; Omi, H.; Adachi, S.; Gotoh, H. Effect of isotopic purification on spectral hole narrowing in $^{167}\text{Er}^{3+}$ hyperfine transitions. *Appl. Phys. Express* **2017**, *10*. [[CrossRef](#)]
16. Omi, H.; Tawara, T. Energy transfers between Er^{3+} ions located at the two crystallographic sites of Er_2O_3 grown on Si(111). *Jpn. J. Appl. Phys.* **2012**, *51*. [[CrossRef](#)]
17. Tawara, T.; Omi, H.; Hozumi, T.; Kaji, R.; Adachi, S.; Goto, H.; Sogawa, T. Population dynamics in epitaxial Er_2O_3 thin films grown on Si(111). *Appl. Phys. Lett.* **2013**, *102*. [[CrossRef](#)]
18. Omi, H.; Tawara, T.; Hozumi, T.; Kaji, R.; Adachi, S.; Gotoh, H.; Sogawa, T. Molecular beam epitaxy of $(\text{Er}_x\text{Sc}_{1-x})_2\text{O}_3$ in Si(111). In Proceedings of the International Conference on Photonics, Optics and Laser Technology (PHOTOPTICS 2014), Lisbon, Portugal, 7–9 January 2014.
19. Adachi, S.; Kawakami, Y.; Kaji, R.; Tawara, T.; Omi, H. Energy transfers in telecommunication-band region of $(\text{Sc},\text{Er})_2\text{O}_3$ thin films grown on Si(111). *J. Phys. Conf. Ser.* **2015**, *647*. [[CrossRef](#)]
20. Tawara, T.; Kawakami, Y.; Omi, H.; Kaji, R.; Adachi, S.; Goto, H. Mechanism of concentration quenching in epitaxial $(\text{Er}_x\text{Sc}_{1-x})_2\text{O}_3$ thin layers. *Opt. Mater. Express* **2017**, *7*, 1097–1104. [[CrossRef](#)]
21. Gruber, J.B.; Nash, K.L.; Sardar, D.K.; Valiev, U.V.; Ter-Gabrielyan, N.; Merkle, L.D. Modeling optical transitions of $\text{Er}^{3+}(4f^{11})$ in C_2 and C_{3i} sites in polycrystalline Y_2O_3 . *J. Appl. Phys.* **2008**, *104*. [[CrossRef](#)]
22. Wybourne, B.G.; Smentek, L. *Optical Spectroscopy of Lanthanides: Magnetic and Hyperfine Interactions*; CRC Press: New York, NY, USA, 2007; ISBN 13-978-1-4200-0693-3.
23. Johnson, L.F.; Guggenheim, H.J.; Rich, T.C.; Ostermayer, F.W. Infrared-to-Visible Conversion by Rare-Earth Ions in Crystals. *J. Appl. Phys.* **1972**, *43*, 1125–1137. [[CrossRef](#)]
24. Van der Ziel, J.P.; Van Uiter, L.G.; Grodkiewicz, W.H.; Mikulyak, R.M. 1.5- μm infrared excitation of visible luminescent in $\text{Y}_{1-x}\text{Er}_x\text{F}_3$ and $\text{Y}_{1-x-y}\text{Er}_x\text{Tm}_y\text{F}_3$ via resonant-energy transfer. *J. Appl. Phys.* **1986**, *60*, 4262–4267. [[CrossRef](#)]
25. Lüthi, S.R.; Pollnau, M.; Gudel, H.U.; Hehlen, M.P. Near-infrared to visible upconversion in Er^{3+} -doped $\text{Cs}_3\text{Lu}_2\text{Cl}_9$, $\text{Cs}_3\text{Lu}_2\text{Br}_9$, and $\text{Cs}_3\text{Y}_2\text{I}_9$ excited at 1.54 μm . *Phys. Rev. B* **1999**, *60*, 162–178. [[CrossRef](#)]
26. Pollnau, M.; Gamelin, D.R.; Lüthi, S.R.; Gudel, H.U.; Hehlen, M.P. Power dependence of upconversion luminescence in lanthanide and transition-metal-ion systems. *Phys. Rev. B* **2000**, *61*, 3337–3346. [[CrossRef](#)]
27. Lupei, A.; Lupei, V.; Gheorghe, C.; Ikesue, A. Excited States Dynamics of Er^{3+} in Sc_2O_3 Ceramic. *J. Lumin.* **2008**, *128*, 918–920. [[CrossRef](#)]
28. Lupei, A.; Lupei, V.; Gheorghe, C.; Ikesue, A.; Osias, E. Upconversion emission of RE^{3+} in Sc_2O_3 ceramic under 800 nm pumping. *Opt. Mater.* **2009**, *31*, 744–749. [[CrossRef](#)]
29. Zheng, K.; Zhao, D.; Zhang, D.; Liu, N.; Qin, W. Ultraviolet upconversion fluorescence of Er^{3+} induced by 1560 nm laser excitation. *Opt. Lett.* **2010**, *35*, 2442–2444. [[CrossRef](#)] [[PubMed](#)]
30. Auzel, F. Up-conversion in RE-doped Solids. In *Spectroscopic Properties of Rare Earths in Optical Materials*; Liu, G., Jacquier, B., Eds.; Springer: Berlin, Germany, 2005.
31. Michael, C.P.; Yuen, H.B.; Sabnis, V.A.; Johnson, T.J.; Sewell, R.; Smith, R.; Jamora, A.; Clark, A.; Semans, S.; Atanackovic, P.B.; et al. Growth, processing, and optical properties of epitaxial Er_2O_3 on silicon. *Opt. Express* **2008**, *16*, 19649–19666. [[CrossRef](#)] [[PubMed](#)]
32. Förster, T. Energy transfer and fluorescence between molecules. *Ann. Phys.* **1948**, *437*, 55–75. [[CrossRef](#)]
33. Dexter, D.L. A theory of sensitized luminescence in solids. *J. Chem. Phys.* **1953**, *21*, 836–850. [[CrossRef](#)]

34. Krupke, W.F.; Shinn, M.D.; Marion, J.E.; Caird, J.A.; Stokowski, S.E. Spectroscopic, optical, and thermomechanical properties of neodymium- and chromium-doped gadolinium scandium gallium garnet. *J. Opt. Soc. Am. B* **1986**, *3*, 102–114. [[CrossRef](#)]
35. Sardar, D.K.; Gruber, J.B.; Zandi, B.; Hutchinson, J.A.; Trussell, C.W. Judd-Ofelt analysis of the Er^{3+} ($4f^{11}$) absorption intensities in phosphate glass: Er^{3+} , Yb^{3+} . *J. Appl. Phys.* **2003**, *93*, 2041–2046. [[CrossRef](#)]
36. Gheorghe, C.; Georgescu, S.; Lupei, V.; Lupei, A.; Ikesue, A. Absorption intensities and emission cross section of Er^{3+} in Sc_2O_3 transparent ceramics. *J. Appl. Phys.* **2008**, *103*. [[CrossRef](#)]
37. Feldmann, J.; Peter, G.; Göbel, E.O.; Dawson, P.; Moore, K.; Foxon, C.; Elliott, R.J. Linewidth dependence of radiative exciton lifetimes in quantum wells. *Phys. Rev. Lett.* **1987**, *59*, 2337–2340. [[CrossRef](#)] [[PubMed](#)]
38. Reisfeld, R. Radiative and non-radiative transitions of rare-earth ions in glasses. In *Structure and Bonding Vol. 22*; Springer: Berlin, Germany, 1975; pp. 123–175.
39. Inokuti, M.; Hirayama, F. Influence of energy transfer by the exchange mechanism on donor luminescence. *J. Chem. Phys.* **1965**, *43*, 1978–1989. [[CrossRef](#)]
40. Cai, M.; Zhou, B.; Wang, F.; Wei, T.; Tian, Y.; Zhou, J.; Xu, S.; Zhang, J. R_2O_3 (R = La, Y) modified erbium activated germanate glasses for mid-infrared 2.7 μm laser materials. *Sci. Rep.* **2015**, *5*. [[CrossRef](#)] [[PubMed](#)]



© 2018 by the authors. Licensee MDPI, Basel, Switzerland. This article is an open access article distributed under the terms and conditions of the Creative Commons Attribution (CC BY) license (<http://creativecommons.org/licenses/by/4.0/>).